Formation of Bismuth Doped Cerium Oxide Nanopowder with Thermal Stability and UV Absorption Properties

Safira Arta Paramita
Department of Physics, Faculty of Science and Mathematics, Universitas Diponegoro

Nurhasanah, Iis
Department of Physics, Faculty of Science and Mathematics, Universitas Diponegoro

Astuti, Yayuk
Department of Chemistry, Faculty of Science and Mathematics, Universitas Diponegoro

Khumaeni, Ali
Department of Physics, Faculty of Science and Mathematics, Universitas Diponegoro

https://doi.org/10.5109/7236862

出版情報：Evergreen. 11 (3), pp.2186-2192, 2024-09. Interdisciplinary Graduate School of Engineering Sciences, Kyushu University, Japan
バージョン：

Formation of Bismuth Doped Cerium Oxide Nanopowder with Thermal Stability and UV Absorption Properties

Safira Arta Paramita[1], Iis Nurhasanah[1,*] Yayuk Astuti[2], Ali Khumaeni[1]
[1]Department of Physics, Faculty of Science and Mathematics, Universitas Diponegoro, Indonesia
[2]Department of Chemistry, Faculty of Science and Mathematics, Universitas Diponegoro, Indonesia

*Author to whom correspondence should be addressed:
E-mail: nurhasanah@fisika.fsm.undip.ac.id

(Received October 29, 2023: Revised June 11, 2024: Accepted June 21, 2024).

Abstract: Among the lanthanide oxides, cerium oxide has superior physicochemical characteristics. The incorporating trivalent dopant proposed to modify the physicochemical characteristics of cerium oxide. This study aims to investigate the formation of bismuth-doped cerium oxide nanopowder through the precipitation method calcined at 200°C. The formation and thermal stability of bismuth-doped cerium oxide were confirmed by X-ray diffraction pattern, scanning electron image, and thermogravimetric curve. The ultraviolet absorption properties were analyzed by UV-Vis diffuse reflectance spectroscopy. The analysis of the X-ray diffraction pattern declared the cubic fluorite cerium oxide formation with crystallite sizes of 7 nm. The bismuth-doped cerium oxide is composed of spherical shape particles. Thermogravimetric curves revealed a high thermal stability of bismuth-doped cerium oxide at a temperature above 500°C, as evidenced by the total decrease in mass percentage of 7.76 wt% that corresponds to the evaporation of adsorbed water and hydroxyl molecules. Incorporating bismuth dopant led to broad ultraviolet absorption of cerium oxide at wavelengths between 200 and 400 nm. The result demonstrates the crystalline bismuth-doped cerium oxide possessed high thermal stability and excellent ultraviolet absorption properties.

Keywords: cerium oxide; bismuth; nanopowder; thermal stability; ultraviolet absorption

1. Introduction

Cerium oxide (CeO_2) is a lanthanide oxide with superior physicochemical characteristics. CeO_2 has high chemical and excellent thermal stability, low toxicity, and biocompatibility[1,2]. Cerium can exist in two valence states, 4+ and 3+, whereas most rare earth metals do not show this characteristic. The valence state 4+ is more stable than 3+ and can exist in the bulk state sub-oxidation CeO_2 formed by a structure of face-centered cubic fluorite (FCC)[3]. Ce^{4+} and Ce^{3+} states are the most attractive properties of CeO_2[4,5]. These states resulted in the oxygen vacancy important for various applications such as solar cells[6,7], fuel oxidation catalysis[8,9], anticorrosion[10,11], and UV absorber[12–14]. Due to its relatively small bandgap compared to ZnO and TiO_2, CeO_2 is an excellent UV absorber widely used in sunscreens[15,16], textiles[17] fibers[18], paints, etc.[19,20]. The bandgap of CeO_2 is strongly affected by the particle size and the crystal defects, such as oxygen vacancy[21]. The tiny particles tend to broaden the absorption bands toward the visible region. Strong UV absorption and high thermal stability became excellent properties as a UV absorber. This advantage makes CeO_2 suitable for UV protection applications[22,23].

To alter the oxygen vacancy of CeO_2, trivalent elements such as gadolinium (Gd), yttrium (Yt), and bismuth (Bi) have been used as dopant sources. Based on simulations by Lucid et al, the Bi^{3+} dopant can increase the crystal structure stability of CeO_2 due to larger radii than Ce^{4+} [24,25]. Besides, the addition of dopant can also improve the thermal and chemical stability and exhibit high UV absorption of the crystals[26,27]. On the other hand, CeO_2 in the nanoscale has different physicochemical properties from its bulk form. The melting point of the material decreases with a reduction in size into the nanoscale dimension because of a larger surface area to volume ratio than bulk material[28].

Consequently, the crystalline of CeO_2 can be formed at low temperature [29]. Some literature shows the formation of CeO_2 and Bi-doped CeO_2 nanopowder using chemical processes including hydrothermal[30], sol-gel hydrothermal[31], sol-gel[32] and precipitation[8]. The formation of CeO_2 and Bi-doped CeO_2 crystalline structures using the hydrothermal method requires a long heating time, while the sol-gel method performs at a very high temperature. Among those methods, precipitation is a simple process, low cost, and time-saving. In addition, CeO_2 crystalline can be produced at a low temperature by combining the precipitation process with ultrasonic radiation[33].

This study describes CeO_2 and Bi-doped CeO_2 nanopowder formation through the precipitation method combined with ultrasonic irradiation. X-ray diffraction pattern identified the crystal structure of CeO_2 and Bi-doped CeO_2. Morphology and an atomic composition contained in CeO_2 were analyzed using scanning electron microscope-energy dispersive X-ray analysis (SEM-EDX). The particle size distribution was determined using transmission electron microscopy images (TEM). The thermal stability of CeO_2 and Bi-doped CeO_2 was observed using a thermogravimetric analysis. The UV absorption of CeO_2 was studied by UV-Vis diffuse reflectance spectroscopy.

2. Experimental

The formation of CeO_2 was carried out by combining ultrasonic radiation and precipitation process[25]. The mixed solvent of demineralized water and isopropanol (Merck) was used to prepare $Ce(NO_3)_3$•$6H_2O$ (Sigma-Aldrich, 99%) solution. To precipitate, a cerium nitrate solution was mixed with 3M ammonium hydroxide (Merck) precipitant until pH 10. Ultrasonic radiation is then applied to the solution. The precipitate was left overnight and washed using distilled water and ethanol. Subsequently, the product of precipitation was calcined at a temperature of 200℃ for 3 hours. The same procedure was used to synthesize Bi-doped CeO_2 by adding $Bi(NO_3)_3$•$5H_2O$ (Sigma-Aldrich, 99%) with a molar ratio of 5%. The structure and crystallinity of the precipitation product were identified by an X-ray diffractometer (Rigaku MiniFlex). The crystallite size (D) was calculated using Equation (1). While the lattice parameter (a) was determined using Equation (2).

$$D = \frac{k\lambda}{\beta \cos\theta} \qquad (1)$$

Where k represents a constant of 0.89, λ denotes the wavelength of the Cu-Kα radiation, θ expresses the angle of Bragg reflection, and β state the full width at half maximum (FWHM).

$$a = \frac{\lambda\sqrt{h^2 + k^2 + l^2}}{2\sin\theta} \qquad (2)$$

Where, h, k, and l sign Miller indices. The morphology and atomic composition of CeO_2 was monitored by scanning electron microscope-energy dispersive X-ray (SEM-EDX) (JEOL JSM-6510LA) and the particle size distribution was estimated from transmission electron microscopy images (TEM) (Talos F200X). The thermal property of CeO_2 was evaluated using a thermal gravimetric analyzer (TGA) (Hitachi STA-200RV). The light absorption properties were analyzed in the 200-800 nm range using UV-Vis diffuse reflectance spectroscopy (Shimadzu). The Kubelka-Munk Equation (3) confirmed the bandgap energy by extrapolating the linear part of $(F(R)hv)^{1/2}$ vs hv (photon energy) curve.

$$(F(R)hv)^{1/2} = A(hv - E_g) \qquad (3)$$

$F(R)$ is the Kubelka-Munk factor, R is the reflectance, hv denotes the photon energy, and A represents a constant.

3. Result and Discussion

3.1 Crystal Structure

The XRD patterns of undoped CeO_2 and Bi-doped CeO_2 produced using the precipitation method are shown in Fig. 1. Both undoped and Bi-doped CeO_2 exhibited several peaks, consistent with the face-centered cubic (FCC) of CeO_2 (JCPDS 34-0394). The crystal planes, 2θ, and FWHM of the XRD pattern are summarized in Table 1.

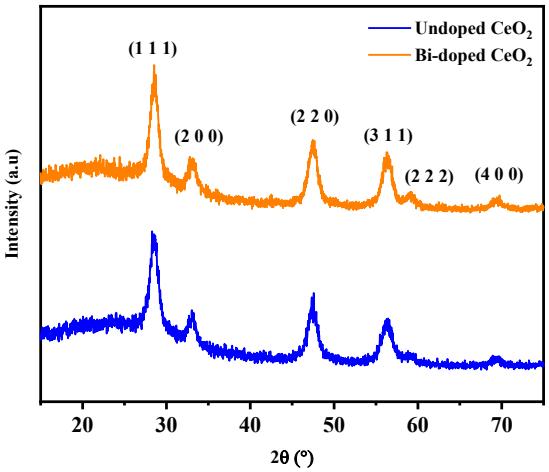

Fig. 1: X-ray diffraction pattern of undoped CeO_2 and Bi-doped CeO_2

In general, it is seen that the diffraction peak of Bi-doped CeO_2 shifted to a larger 2θ and the FWHM value increased. This indicates that Bi dopant has been substituted into the lattice of CeO_2. Both undoped and Bi-doped CeO_2 showed a preferred diffraction peak of (111) plane, located at 2θ of 28.53˚ and 28.58˚, respectively. The XRD patterns of Bi-doped CeO_2 do not show any secondary phase, revealing that the substitution of Bi dopant maintained the fluorite structure.

Table 1. The X-ray diffraction data of undoped CeO_2 and Bi-doped CeO_2

h k l	**Undoped-CeO_2**		**Bi-doped CeO_2**	
	2θ (°)	**FWHM (°)**	**2θ (°)**	**FWHM (°)**
1 1 1	28.53	1.12	28.58	1.17
2 0 0	33.06	1.15	33.20	1.24
2 2 0	47.13	1.69	47.53	1.31
3 3 1	56.00	1.57	56.02	1.63
2 2 2	58.77	1.22	58.83	1.51
4 0 0	69.46	1.54	69.20	1.70

The crystallite sizes of 7.24 nm and 6.93 nm were found using Equation (1) for undoped CeO_2 and Bi-doped CeO_2, respectively. The lattice parameter of Bi-doped CeO_2 (5.4146 Å) is almost the same value as undoped CeO_2 (5.4053 Å). The slight difference in both lattice parameters revealed that substituting the Bi dopant does not deform the CeO_2 lattice. The obtained lattice parameter in this study is close to the lattice parameter of CeO_2 reference of cubic fluorite (JCPDS 34-0394) and previous study[8,31,32].

3.2 Morphology

The morphology of undoped CeO_2 and Bi-doped CeO_2 is depicted in Fig. 2. The size and shape of particles in undoped and bi-doped CeO_2 are not significantly different from one another. The nanometric particles are distributed in undoped and Bi-doped CeO_2 indicating the formation of nanopowder. However, there are particles agglomeration or aggregation, and particles of Bi-doped CeO_2 are more dispersed than undoped CeO_2.

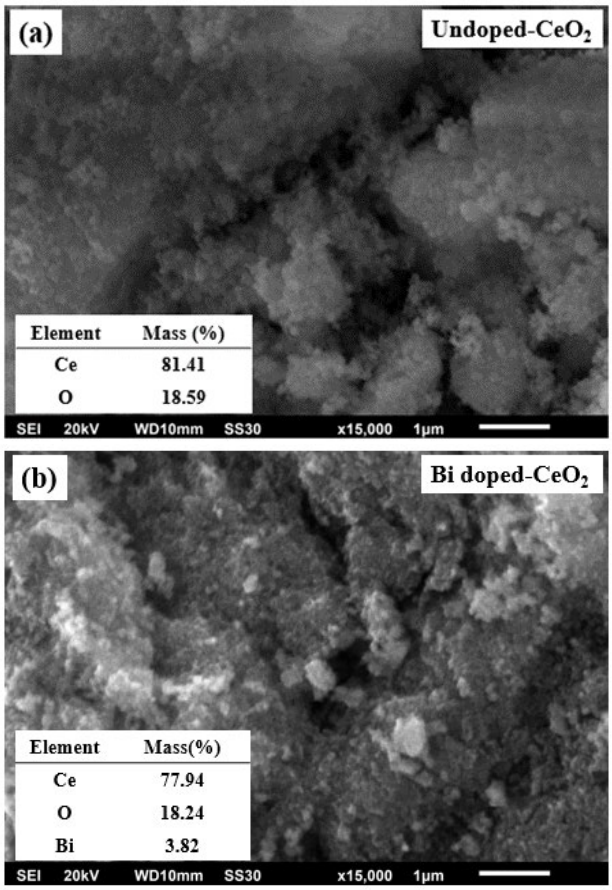

Fig. 2: SEM images of (a) un-doped CeO_2 and (b) Bi-doped CeO_2 (The insert table is atomic composition)

The existing Bi dopant in CeO_2 was analyzed based on the mass percentage of Ce, O, and Bi atoms composition from EDX measurement presented by the white box in the insert Fig. 2. The mass percentages of 81.41% and 18.59% were obtained for Ce and O atoms in undoped CeO_2, respectively, as indicated in Fig. 2(a). This result is close to the stoichiometric composition of Ce (81.39%) and O (18.61%) mass percent atoms. At the same time, Ce and O atoms mass percent contained in Bi-doped CeO_2 were found to be 77.94% and 18.24%, respectively, as depicted in Fig. 2(b). The lower Ce mass percent of Bi-doped CeO_2 than undoped CeO_2 indicated the presence of Bi atom in the CeO_2. The Bi mass percent atom is 3.82% which corresponds to 4.9% concentration of Bi in CeO_2. This result is close to the molar ratio of the Bi source in the prepared synthesis process. The mass percent atom oxygen in both samples is lower than the stoichiometric of CeO_2 revealing the oxygen deviation in the prepared undoped CeO_2 and Bi-doped CeO_2. The oxygen deviation in Bi-doped CeO_2 is higher than another one of undoped CeO_2.

A clearer depiction of particle morphology is achieved through TEM analysis. The TEM image in Fig. 3(a) shows that undoped CeO_2 has cubic shape particles in aggregate formed (pointed by the red cube), while Bi-doped CeO_2 appears composed of spherical particles (pointed by the red circle) in Fig. 3(b). In this case, the spherical shape of Bi-doped CeO_2 particles is more spread evenly than the cubic shape of undoped CeO_2 particles. This characteristic can be correlated to an average particle size of both CeO_2. Smaller particles tend to form aggregate. The average particle sizes of undoped CeO_2 and Bi-doped CeO_2 are 7.86 nm and 16.25 nm, respectively as seen in Fig 4.

The cubic shape of undoped CeO_2 was also observed for synthesized using the same method with dried treatment in a vacuum oven at 110 °C and calcined at 600°C[34]. Bi-doped CeO_2 particle was also detected in CeO_2 synthesized using the sol-gel method at a calcination temperature of 700°C[32]. In contrast to the hydrothermal method which produced undoped CeO_2 and Bi-doped CeO_2 nanorod[30,31].

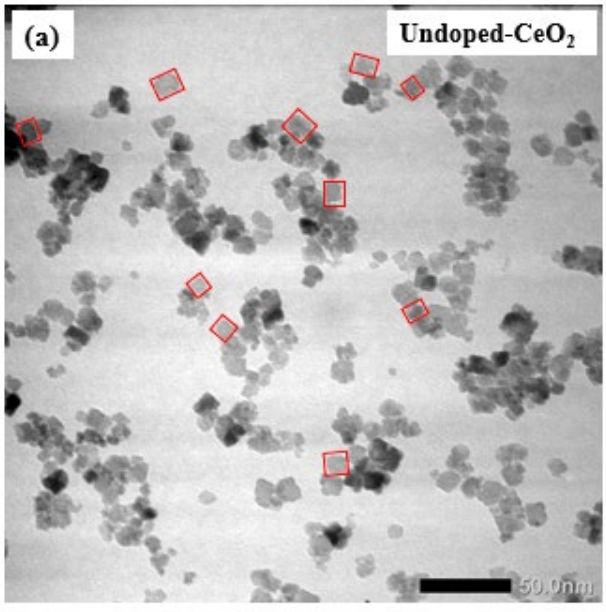

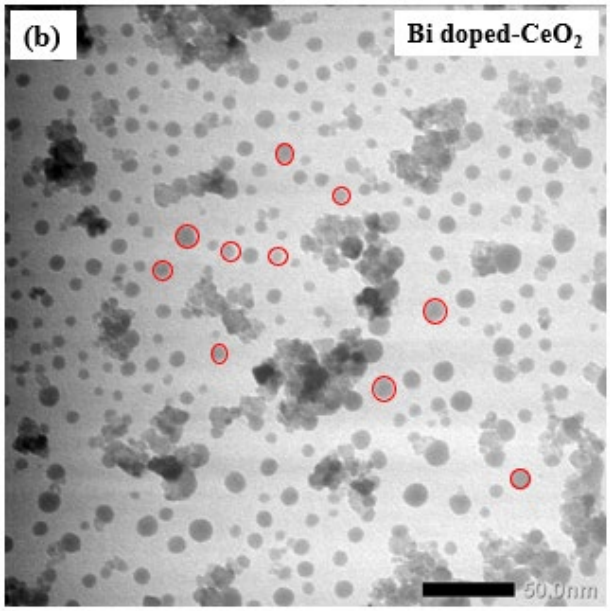

Fig. 3: TEM images of (a) undoped CeO_2, and (b) Bi-doped CeO_2

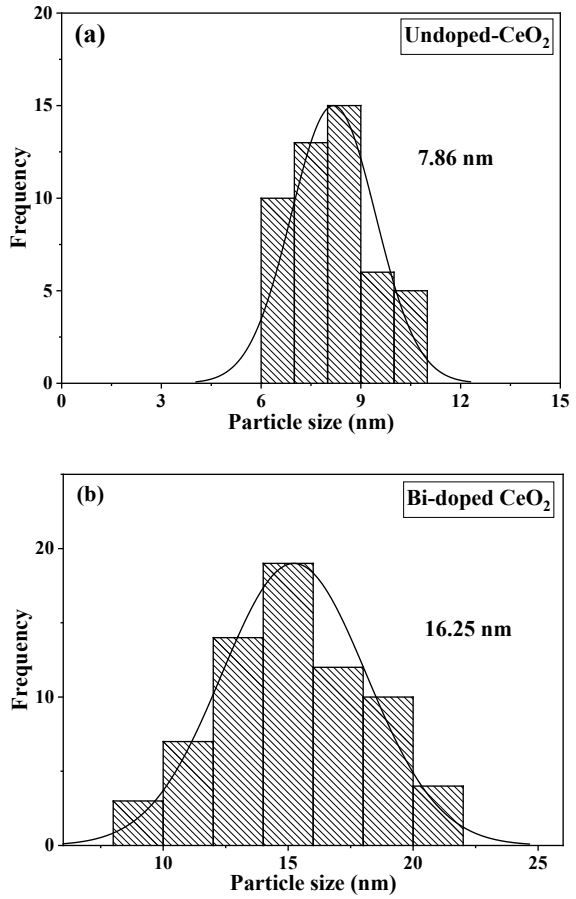

Fig. 4: Particle size distribution of (a) undoped CeO_2 and (b) Bi-doped CeO_2

3.3 Thermal Properties

Thermograms of undoped CeO_2 and Bi-doped CeO_2 were recorded from room temperature to 900°C as shown in Fig. 5. The thermogram curves indicate two weight-loss steps: the first weight-loss step is 3.42 wt% of undoped CeO_2 and 3.51 wt% for Bi-doped CeO_2 started from 24°C and completed at 120°C. These weight losses are related to the removal of adsorbed water. The second inflection point between 120°C and 480°C shows a weight loss of 4.69 wt% and 4.25 wt% for both CeO_2 due to the elimination of hydroxyl molecules. The total weight loss of undoped CeO_2 is 8.11 wt% and Bi-doped CeO_2 is 7.76 wt%. The insertion of Bi dopant provided less weight loss, suggesting that Bi doping improved the formation of stable fluorite cubic CeO_2 crystal.

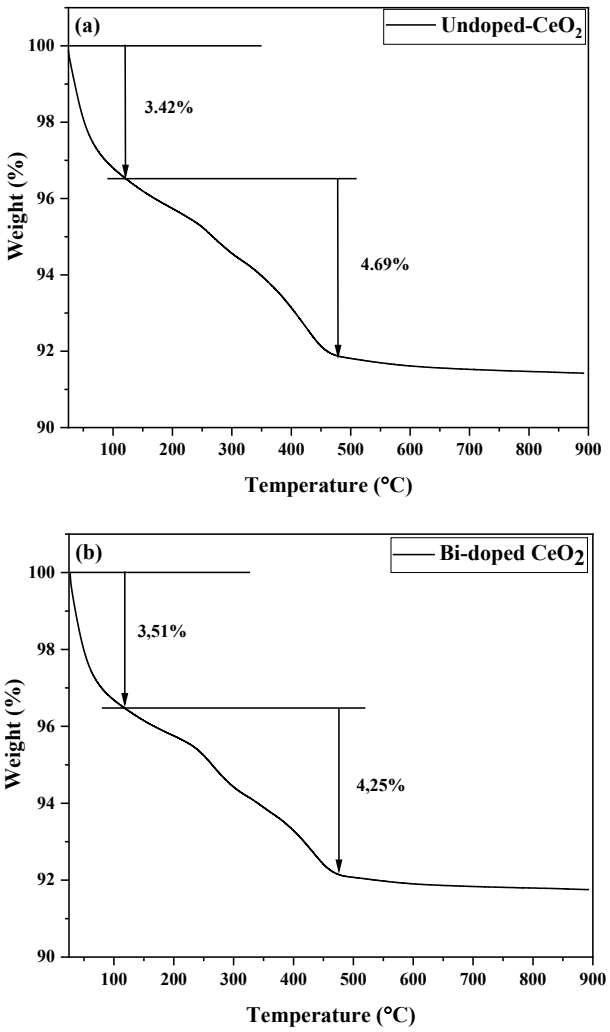

Fig. 5: TGA curve of (a) undoped CeO_2 and (b) Bi-doped CeO_2

In synthesizing CeO_2 using the precipitation method, hydroxyl groups are still trapped in the samples [35]. However, after heating above 480°C, all hydroxyl groups will be lost, and the CeO_2 crystalline formed becomes more stable. The addition of Bi into CeO_2 reduces the presence of trapped hydroxyl molecules, resulting in less weight loss than undoped CeO_2. A slight weight loss in both samples indicates that the CeO_2 formation has been established at a temperature of 200°C. The result is in

agreement with the X-ray diffraction measurement which shows a single phase of CeO_2.

3.4 Optical Properties

The absorbance spectra in the UV-Vis region as shown in Fig. 5, were utilized to evaluate the optical characteristics of undoped CeO_2 and Bi-doped CeO_2. High and broad absorbance appeared at wavelengths between 200 and 400 nm. It shows both CeO_2 possess strong UV absorption that originated from the electronic transition between O 2p and Ce 4f. The insertion of Bi into CeO_2 slightly decreases UV absorbance. Meanwhile, the absorption band edge shifts towards higher wavelengths. This phenomenon is associated with the presence of crystal defects due to Bi doping, resulting in a more yellowish color compared to undoped CeO_2[22]. Accordingly, the Bi-doped CeO_2 absorbance spectrum is broadened.

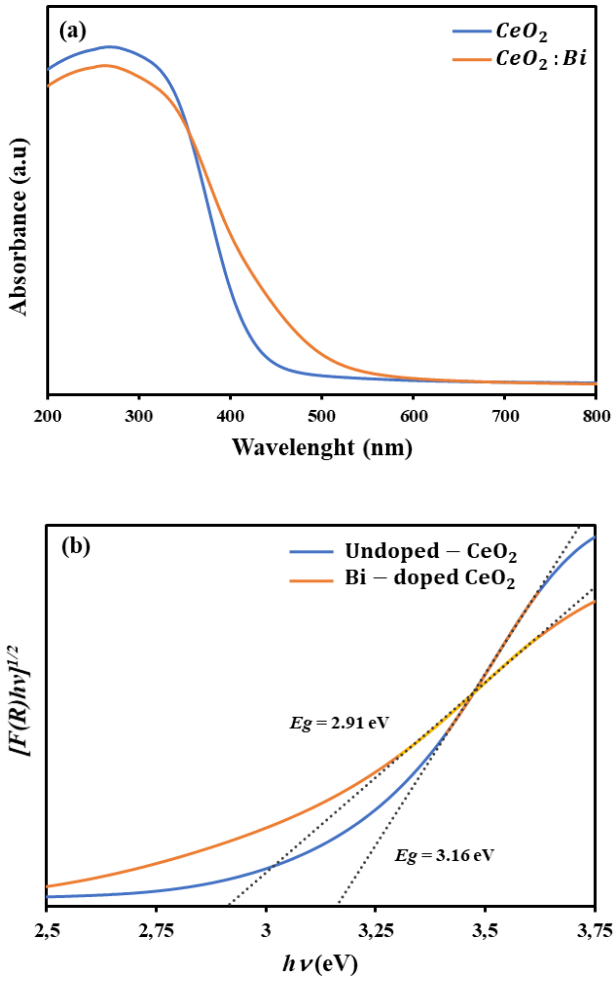

Fig. 5: (a) UV–Vis absorbance spectra and (b) Kubelka–Munk plots of undoped CeO_2 and Bi-doped CeO_2

Furthermore, the bandgap energy was evaluated by using the Kubelka-Munk function. The obtained bandgap energies of undoped CeO_2 and Bi-doped CeO_2 are 3.16 eV and 2.91 eV, respectively. The insertion of Bi leads to a decrease in the bandgap energy and induces a redshift phenomenon as reported by other researchers[31,32]. This study's result agrees with previous studies which demonstrated CeO_2 as a UV absorber[12,19,22].

4. Conclusion

CeO_2 and Bi-doped CeO_2 nanopowder formation was established at a calcination temperature of 200°C using a combination of precipitation method with ultrasound radiation. X-ray diffraction patterns declared a single phase of CeO_2 formation with a cubic fluorite structure. The addition of Bi to CeO_2 changes the shape of CeO_2 particles from cubic to spherical and reduces agglomeration. The thermogravimetric analysis showed a minor weight loss of hydroxyl molecules that were still trapped on the surface of CeO_2 with a total weight loss of 8.11 wt% for undoped CeO_2 and 7.76 wt% for Bi-doped CeO_2. Less weight-loss of Bi-doped CeO_2 than undoped CeO_2 confirmed that Bi dopant improved the thermal stability of CeO_2 crystalline. The shift of the absorption band in Bi-doped CeO_2 to higher wavelengths is attributed to the Bi dopant that increases the yellow color of CeO_2. The undoped CeO_2 and Bi-doped CeO_2 possessed strong UV absorption properties. The high thermal stability and excellent UV absorption suggested undoped CeO_2 and Bi-doped CeO_2 potential for UV protective application.

Acknowledgments

The authors acknowledge that The Ministry of Research and Technology/National Research and Innovation Agency of the Republic of Indonesia (No. 187-29/UN7.6.1/PP/2022) provided financial support.

Nomenclature

E_g	Band gap energy (eV)
FWHM	Full width at half maximum (˚)

Greek symbols

β	FWHM
θ	Bragg angle
ν	frequency of photon
λ	Wavelength

References

1) A. Garzón-Manjón, A. Aranda-Ramos, B. Melara-Benítez, I. Bensarghin, J. Ros, S. Ricart, and C. Nogués, "Simple synthesis of biocompatible stable CeO_2 nanoparticles as antioxidant agents," *Bioconjug. Chem.*, **29** (7) 2325–2331 (2018). doi:10.1021/acs.bioconjchem.8b00300.
2) T.X.T. Sayle, M. Molinari, S. Das, U.M. Bhatta, G. Möbus, S.C. Parker, S. Seal, and D.C. Sayle,

"Environment-mediated structure, surface redox activity and reactivity of ceria nanoparticles," *Nanoscale*, **5** (*13*) 6063–6073 (2013). doi:10.1039/c3nr00917c.

3) H.X. Mai, L.D. Sun, Y.W. Zhang, R. Si, W. Feng, H.P. Zhang, H.C. Liu, and C.H. Yan, "Shape-selective synthesis and oxygen storage behavior of ceria nanopolyhedra, nanorods, and nanocubes," *J. Phys. Chem. B*, **109** (*51*) 24380–24385 (2005). doi:10.1021/jp055584b.
4) S.C. Yang, S.H. Pang, T.P. Sulmonetti, W.N. Su, J.F. Lee, B.J. Hwang, and C.W. Jones, "Synergy between ceria oxygen vacancies and Cu nanoparticles facilitates the catalytic conversion of CO_2 to CO under mild conditions," *ACS Catal.*, **8** (*12*) 12056–12066 (2018). doi:10.1021/acscatal.8b04219.
5) M. Noor, M.A. Al Mamun, A.K.M. Atique Ullah, A. Matsuda, G. Kawamura, M.A. Hakim, M.F. Islam, and M.A. Matin, "Physics of $Ce^{3+}\leftrightarrow Ce^{4+}$ electronic transition in phytosynthesized $CeO_2/CePO_4$ nanocomposites and its antibacterial activities," *J. Phys. Chem. Solids*, **148** (2021). doi:10.1016/j.jpcs.2020.109751.
6) A. Corma, P. Atienzar, H. García, and J.Y. Chane-Ching, "Hierarchically mesostructured doped CeO_2 with potential for solar-cell use," *Nat. Mater.*, **3** (*6*) 394–397 (2004). doi:10.1038/nmat1129.
7) A. Rajendran, and S. Kandasamy, "Synthesis and photovoltaic property characterization of CeO_2 film deposited on ITO substrate for dye sensitized solar cell," *Mater. Res. Innov.*, **23** (*1*) 15–21 (2019). doi:10.1080/14328917.2017.1349060.
8) S.C. Hebert, and K. Stöwe, "Synthesis and characterization of bismuth-cerium oxides for the catalytic oxidation of diesel soot," *Materials*, **13** (*6*) (2020). doi:10.3390/ma13061369.
9) Y. Egawa, S. Hamada, and H. Einaga, "Contribution of catalytic performance of CeO_2 in nonthermal plasma chemical reaction," *Evergreen*, **5** (*3*) 34–37 (2018). doi:10.5109/1957498.
10) K. Dinesh, S. Satnam, and A. Surjit, "Morphology and Corrosion Behavior of Stir-Cast Al6061-CeO_2 Nanocomposite Immersed in NaCl and H_2SO_4 Solutions," *Evergreen*, **10** (*1*) 94-104 (2023). doi.org/10.5109/6781054
11) K. An, Y. Sui, Y. Qing, C. Yang, C. Long, L. Wang, and C. Liu, "Synergistic reinforcement coating with anti-corrosion and UV aging resistance by filling modified CeO_2 nanoflakes," *Colloids Surf. A: Physicochem. Eng. Asp.*, **625** (2021). doi:10.1016/j.colsurfa.2021.126904.
12) Z. Lu, C. Mao, M. Meng, S. Liu, Y. Tian, L. Yu, B. Sun, and C.M. Li, "Fabrication of CeO_2 nanoparticle-modified silk for UV protection and antibacterial applications," *J Colloid Interface Sci.*, **435** 8–14 (2014). doi:10.1016/j.jcis.2014.08.015.
13) R. Kumar, Sujit Kumar Verma, Naveen Kumar Gupta, and Santosh Kumar Singh, "Performance enhancement of TSAH using graphene and graphene/CeO_2-black paint coating on absorber: a comparative study," *Evergreen*, **9** (*3*) 673–681 (2022). doi:10.5109/4843098.
14) N. Ditlopo, N. Sintwa, S. Khamlich, E. Manikandan, K. Gnanasekaran, M. Henini, A. Gibaud, A. Krief, and M. Maaza, "From Khoi-San indigenous knowledge to bioengineered CeO_2 nanocrystals to exceptional UV-blocking green nanocosmetics," *Sci. Rep.*, **12** (*1*) (2022). doi:10.1038/s41598-022-06828-x.
15) S. Parwaiz, M.M. Khan, and D. Pradhan, "CeO_2-based nanocomposites: an advanced alternative to TiO_2 and ZnO in sunscreens," *Materials Express*, **9** (*3*) 185–202 (2019). doi:10.1166/mex.2019.1495.
16) Z. Li, L. Tong, Y. Ma, and L. Zhao, "Fabrication of CeO_2/CaO nanocomposite as ultraviolet screening agent and its application in sunscreen," *Ceram Int*, **50** (*11*) 20431–20440 (2024). doi:10.1016/j.ceramint.2024.03.166.
17) I.H. Dwirekso, M. Ibadurrohman, and Slamet, "Synthesis of TiO_2-SiO_2-CuO nanocomposite material and its activities for self-cleaning," *Evergreen*, **7** (*2*) 285–291 (2020). doi:10.5109/4055234.
18) H.M. Chenari, L. Riasvand, and S. Khalili, "The synthesis condition and characterization of thermally treated CeO_2 and ZnO–CeO_2 composite fibers," *Ceram. Int.*, **45** (*11*) 14223–14228 (2019). doi:10.1016/j.ceramint.2019.04.130.
19) W. Duan, A. Xie, Y. Shen, X. Wang, F. Wang, Y. Zhang, and J. Li, "Fabrication of superhydrophobic cotton fabrics with UV protection based on CeO_2 particles," *Ind. Eng. Chem. Res.*, **50** (*8*) 4441–4445 (2011). doi:10.1021/ie101924v.
20) A. Iqbal, A.S. Ahmed, N. Ahmad, A. Shafi, T. Ahamad, M.Z. Khan, and S. Srivastava, "Biogenic synthesis of CeO_2 nanoparticles and its potential application as an efficient photocatalyst for the degradation of toxic amido black dye," *Environ. Nanotechnol. Monit. Manag.*, **16** (2021). doi:10.1016/j.enmm.2021.100505.
21) M.M. Khan, S.A. Ansari, D. Pradhan, D.H. Han, J. Lee, and M.H. Cho, "Defect-induced band gap narrowed CeO_2 nanostructures for visible light activities," *Ind. Eng. Chem. Res.*, **53** (*23*) 9754–9763 (2014). doi:10.1021/ie500986n.
22) M. Aklalouch, A. Calleja, X. Granados, S. Ricart, V. Boffa, F. Ricci, T. Puig, and X. Obradors, "Hybrid sol-gel layers containing CeO_2 nanoparticles as uv-protection of plastic lenses for concentrated photovoltaics," *Sol. Energy Mater. Sol. Cells*, **120** (*PART A*) 175–182 (2014). doi:10.1016/j.solmat.2013.08.040.
23) H. Li, P. Xia, S. Pan, Z. Qi, C. Fu, Z. Yu, W. Kong, Y. Chang, K. Wang, D. Wu, and X. Yang, "The advances

of ceria nanoparticles for biomedical applications in orthopaedics," *Int. J. Nanomedicine*, **15** 7199–7214 (2020). doi:10.2147/IJN.S270229.

24) A.K. Lucid, P.R.L. Keating, J.P. Allen, and G.W. Watson, "Structure and reducibility of CeO_2 doped with trivalent cations," *J. Phys. Chem. C*, **120** (*41*) 23430–23440 (2016). doi:10.1021/acs.jpcc.6b08118.
25) S. Patil, S. Seal, Y. Guo, A. Schulte, and J. Norwood, "Role of trivalent La and Nd dopants in lattice distortion and oxygen vacancy generation in cerium oxide nanoparticles," *Appl. Phys. Lett.*, **88** (*24*) (2006). doi:10.1063/1.2210795.
26) A. Miri, and M. Sarani, "Biosynthesis, characterization and cytotoxic activity of CeO_2 nanoparticles," *Ceram. Int.*, **44** (*11*) 12642–12647 (2018). doi:10.1016/j.ceramint.2018.04.063.
27) M. Kohantorabi, and M.R. Gholami, "Fabrication of novel ternary Au/CeO_2@g-C_3N_4 nanocomposite: kinetics and mechanism investigation of 4-nitrophenol reduction, and benzyl alcohol oxidation," *Appl. Phys. A Mater. Sci. Process*, **124** (*6*) (2018). doi:10.1007/s00339-018-1858-0.
28) A.C. Opia, M.K.A. Hamid, S. Samion, C.A.N. Johnson, A.B. Rahim, and M.B. Abdulrahman, "Nano-particles additives as a promising trend in tribology: a review on their fundamentals and mechanisms on friction and wear reduction," *Evergreen*, **8** (*4*) 777–798 (2021). doi:10.5109/4742121.
29) M. Singh, S. Lara, and S. Tlali, "Effects of size and shape on the specific heat, melting entropy and enthalpy of nanomaterials," *J. Taibah Univ. Sci.*, **11** (*6*) 922–929 (2017). doi:10.1016/j.jtusci.2016.09.011.
30) Y. Liu, M. Wang, M. Shen, Q. Wang, and L. Zhang, "Bi-doped ceria with increased oxygen vacancy for enhanced CO_2 photoreduction performance," *Wuji Cailiao Xuebao/J. Inorg. Mater.*, **36** (*1*) 88–94 (2021). doi:10.15541/jim20200142.
31) D. Jiang, W. Wang, E. Gao, L. Zhang, and S. Sun, "Bismuth-induced integration of solar energy conversion with synergistic low-temperature catalysis in $Ce_{1-x}Bi_xO_{2-\delta}$ nanorods," *J. Phys. Chem. C*, **117** (*46*) 24242–24249 (2013). doi:10.1021/jp4092943.
32) C. Santra, A. Auroux, and B. Chowdhury, "Bi doped CeO_2 oxide supported gold nanoparticle catalysts for the aerobic oxidation of alcohols," *RSC Adv.*, **6** (*51*) 45330–45342 (2016). doi:10.1039/c6ra05216a.
33) A.F. Efendi, and I. Nurhasanah, "UV-Light absorption and photocatalytic properties of Zn-doped CeO_2 nanopowders prepared by ultrasound irradiation," *Mater. Sci. Forum*, *827*: 56–61 (2015). doi:10.4028/www.scientific.net/MSF.827.56.
34) M. Ramachandran, R. Subadevi, and M. Sivakumar, "Role of PH on synthesis and characterization of cerium oxide (CeO_2) nano particles by modified co-precipitation method," *Vacuum*, **161** 220–224 (2019). doi:10.1016/j.vacuum.2018.12.002.
35) A.A. Ansari, and A. Kaushik, "Synthesis and optical properties of nanostructured $Ce(OH)_4$," *J. Semiconductors*, **31** (*3*) (2010). doi:10.1088/1674-4926/31/3/033001.